RESEARCH

Optical Properties of Multiple Fano Resonance in MIM Waveguide System Coupled with a Semi-Elliptical Ring Resonator

Mustapha Figuigue[1] · Oussama Mahboub[1] · Rida El Haffar[1]

Abstract

A metal-insulator-metal (MIM) waveguide structure consists of semi-elliptical ring resonator (SERR) and a baffle was proposed and numerically investigated by using the finite element method (FEM). By changing the geometrical parameters such as the radii of SERR and the width of the baffle, the transmission characteristics and line shape can be easily tuned. The simulation results show that the proposed plasmonic system is used as a sensor by filling the insulator region with different refractive index. The sensitivity and figure of merit of this sensor can reach 1783 nm/RIU and 27, respectively. It is found that the proposed structure exhibits a slow light effect, and it is shown that the optical delay achieved is 0.887 ps. The results clarified that the developed structure could have a great potential in nanosensor devices and slow light systems.

Keywords Surface plasmons SPPs · Fano resonance · Metal-Insulator-Metal (MIM) waveguides · Plasmonic sensors · Refractive index

Introduction

Surface plasmon polaritons (SPPs) are electromagnetic waves in the form of collective oscillations, which are generated by the interaction between incident light and free electrons on the metal surface; it can propagate along the metal/dielectric interface with an exponential decay in the direction perpendicular to this interface [1, 2]. Having the perfect characteristics of breaking the diffraction limit of light and controlling optical signal propagation at the nanoscale [3], SPPs are very promising for applications in highly integrated photonic circuits and optical devices [4–6]. In particular, metal-insulator-metal (MIM) waveguides based on SPPs have deep subwavelength field confinements and low bending loss. What is more, this type of waveguide presents strong local field enhancement characteristics, long propagation length, and easy integration at the nanoscale, which make them very promising for the realization of potential applications in highly integrated nanophotonic circuits. Many MIM waveguide-based optical devices consisting of waveguides and resonators have

been investigated, such as plasmonic sensors [7, 8], filters [9–11], and splitters [12]. Resonators coupled to a MIM waveguide can produce special optical effects such as electromagnetically induced transparency (EIT) [13] and its analog [14] which is the Fano resonance [15, 16]. The asymmetric Fano resonance is a particular optical phenomenon of interacting quantum systems, which arises from the interference between a continuous state band and a discrete quantum state [17]. Systems that excite Fano resonances are very sensitive to the surrounding environment in a specific frequency range, exhibiting faster optical responses and high local field enhancement. In contrast to the Lorentzian line resonance, the Fano resonance exhibits a typical sharp and asymmetric line profile [18] and due to the high dispersion of the Fano resonance curves is receiving special attention and many nanostructures have been proposed for optical applications in miniature sensors [19, 20], optical switches [21, 22], all-optical logic gates [6], slow light devices [23, 24], and wavelength demultiplexing systems [25, 26]. In recent years, many Fano resonance systems based on MIM waveguide structures coupled with double side-coupled slot cavities or double parallel slots [27, 28] have been designed. For example, Hua Lu et al. [29] proposed a dual-array resonator coupling structure. Ouyang et al. proposed and studied the tunable Fano resonance in MIM waveguide structure coupled with

✉ Rida El Haffar
ridahaffar@gmail.com

1   National School of Applied Sciences (ENSATe),
     Abdelmalek Essaadi University, Tetouan, Morocco

hetero-cavities [30]. Meng et al. investigated the control of Fano resonance in photonic crystal nanobeams coupled with nanobeam cavities and its application in detection [31]. Houlin An et al. [32] designed two MIM waveguide structures consisting of a cavity and a T-type deflector. In addition, several tunable Fano resonances were first realized in an end-coupled system consisting of a rectangular cavity and an inverted U-shaped slot by Fang et al. [33]. In this paper, a novel compact refractive index nano-sensor is proposed and numerically investigated. For this sensor, the designed structure is composed of a baffle coupled to a semi-elliptical ring resonator (SERR).

There are some reasonable motivations to choose the SERR resonator shape. Firstly, in the elliptical shape, the different optical resonance tuning scenarios are likely to be compared to the other shapes; thus, the performance of the device can be tuned by adjusting the major and minor radii of the elliptical shape. Elliptical resonators offer a higher coupling coefficient and quality factor than the majority of earlier resonator systems using MIM waveguide, making them preferred for slow light devices [34]. Additionally, the substantial energy loss in the corners of acute angle resonators can limit their use; however, by rounding the corners and selecting an ideal radius of curvature, this energy loss can be reduced [35, 36]. Finally, the different fabrication technics of an elliptical geometry can be easier and accurate compared to the fabrication process of shapes with corners like rectangular and triangular shapes [37, 38]. Regarding the nanofabrication of plasmonic components, Stade et al. [39] and Campos et al. [40] have demonstrated the experimental fabrication of nanostructures with dimensions on the same scale and even less of the studied device. Bozhevolnyi et al. studied experimentally the Channel plasmon subwavelength waveguide components [41]. The fabrication methods used for such devices with high resolution are focused ion beam milling (FIB) [42], electron beam lithography (EBL) [43], or nanoimprint lithography (NIL). The latter option can be considered an excellent choice for both commercial and academic applications due to its cost-effectiveness and high throughput capabilities [44].

In this work, the peaks of multiple Fano resonances are obtained using a compact MIM waveguide structure. Both the narrow-band "bright" modes and the broad-band "dark" modes are switched on because the SERR operates as a Fabry-Perot (FP) resonator and the baffle (slot) has the potential to function as a reflector. The Fano resonance arises from interactions between these two modes. In respect to the geometrical parameters of SERR, we present an investigation of their effects on optical characteristics of the proposed structure like the optical delay to evaluate slow light effect, and the sensitivity and the figure of merit (FOM) are used to assess the detection properties of the sensor.

Structure Design and Simulation Method

Figure 1 shows the structure of the proposed multiple Fano resonance plasmonic system. It consists of a MIM waveguide edge-coupled to a metal baffle (which is located between the two input and output ports) and side-coupled to a semi-elliptical ring resonator (SERR). The major and minor mean radii of the semi-elliptical resonator are R and r, respectively. The width and height of the baffle are d and w, respectively. For the entire article, the MIM waveguide's width is fixed, $w = 50\ nm$. The coupling distance between the MIM waveguide and the semi-elliptical resonator is g.

The optical properties in Fig. 1 are investigated numerically using the finite element method (FEM), and the results will be compared initially with the finite difference time domain (FDTD) method. Since the width of the waveguide is significantly smaller ($w = 50\ nm$) than the wavelength of the incident light, the waveguide supports a single TM_0 propagation mode. In this numerical study, a TM-polarized plane wave is injected into the MIM structure, where $((\vec{H}//\vec{Z}))$, i.e., the magnetic field, is perpendicular to the plane of Fig. 1 [6]. While the SPPs waves are forming on the two metal interfaces, the incident light will be coupled into the bus waveguide. A perfectly matched layer (PML) serves as an absorbing boundary condition for the FDTD method in order to absorb the outgoing waves, reduce simulation errors, and minimize sidewall reflections. The simulation parameters are as follows: grid size used in FDTD simulation is set
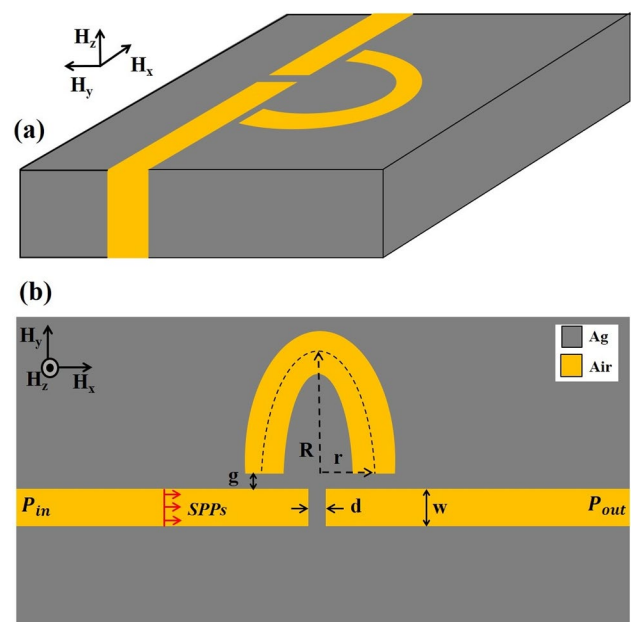

Fig. 1 a 3D Schematic diagram of the MIM waveguide structure composed of a baffle and a SERR resonator. **b** The corresponding 2D view of the proposed structure. The parameters of the structure are as follows: $R = 225\ nm$, $r = 105\ nm$, $d = 10\ nm$, and $g = 10\ nm$

to 2 *nm* to keep convergence, input type: continuous wave field modulated by a Gaussian, simulation time: 1400 *fs*. It is worth noting that all these studies were performed using a two-dimensional (2D) model, since the characteristics of 3D models can be approximately analogous to those of 2D models, assuming that the thickness of the proposed structure in the third dimension is much larger than the size of the element in the design plane (2D) [45]. Therefore, the effect of substrate thickness on the obtained results can be mathematically neglected by assuming that the structure is infinite in the third dimension [46]. In addition, 2D simulations are significantly faster for highly resonant devices without compromising the accuracy of the calculations. In the simulations, the transmission of SPPs from the input port to the output port is calculated using the elements of the system scattering matrix, $T = |S_{21}|^2$, where S_{21} is the transmission coefficient from the input port P_{in} to the output port P_{out}. In this article, a two-dimensional model has been implemented for simplicity's sake, where the yellow and gray areas represent air ($\epsilon_d = 1$) and silver (ϵ_{Ag}), respectively. The permittivity of silver is defined by the Drude model:

$$\epsilon_{Ag} = \epsilon_\infty - \frac{\omega_p^2}{\omega^2 + j\omega\gamma} \tag{1}$$

Here, ϵ_∞ is the dielectric constant at the infinite frequency, and ω_p and γ stand for the bulk plasma frequencies and the electron collision, respectively. ω is the angular frequency of incident light. The parameters for silver can be set as $\epsilon_\infty = 3.7$, $\omega_p = 9.1\,eV$ and $\gamma = 0.018\,eV$ [33].

For the MIM waveguide structures, the dispersion relation for the surface plasmon polaritons (SPPs) supporting the mode can be expressed by the following equation [47]:

$$\epsilon_d\sqrt{(\beta_{spp}^2 - \epsilon_m k_0^2)} + \epsilon_m\sqrt{(\beta_{spp}^2 - \epsilon_d k_0^2)}\tanh(\omega\sqrt{(\beta_{spp}^2 - \epsilon_d k_0^2)}/2) = 0 \tag{2}$$

where $k_0 = 2\pi/\lambda$ is the free-space wave vector, and β_{spp} is the wave vector of SPPs in the MIM waveguide.

The wavelength of the resonant modes of the MIM resonator cavity in the transmission spectra can be obtained approximately by the following analytical model [5]:

$$\lambda \approx \frac{2Re(n_{eff})L_{eff}}{m} \tag{3}$$

where $Re(n_{eff})$ is the real part of the effective refractive index for a wavelength in the MIM waveguide, L_{eff} represents the effective length of the resonator, and m is the order of the resonance mode (m is a positive integer).

To model the optical response of the device structure, we use the commercial solver COMSOL Multiphysics which is based on the FEM method; then, the results are corroborated using the Lumerical FDTD solver which is based on the FDTD method. As shown in Fig. 2a, a baffle is placed in the

middle of the MIM waveguide bus, while a semi-elliptical ring (SERR) is placed on one of the two sides of this waveguide and separated with a coupling distance *g*. The dark mode (narrowband) and a bright mode (broadband) are produced by the SERR ring and the baffle, respectively. Since the last two modes are overlapped, the Fano resonances are generated according to the order of the existing modes.

Simulation Results and Discussion

In order to understand the principle of producing the Fano resonance phenomenon by the proposed overall structure which is shown in Fig. 1, it was spectrally analyzed according
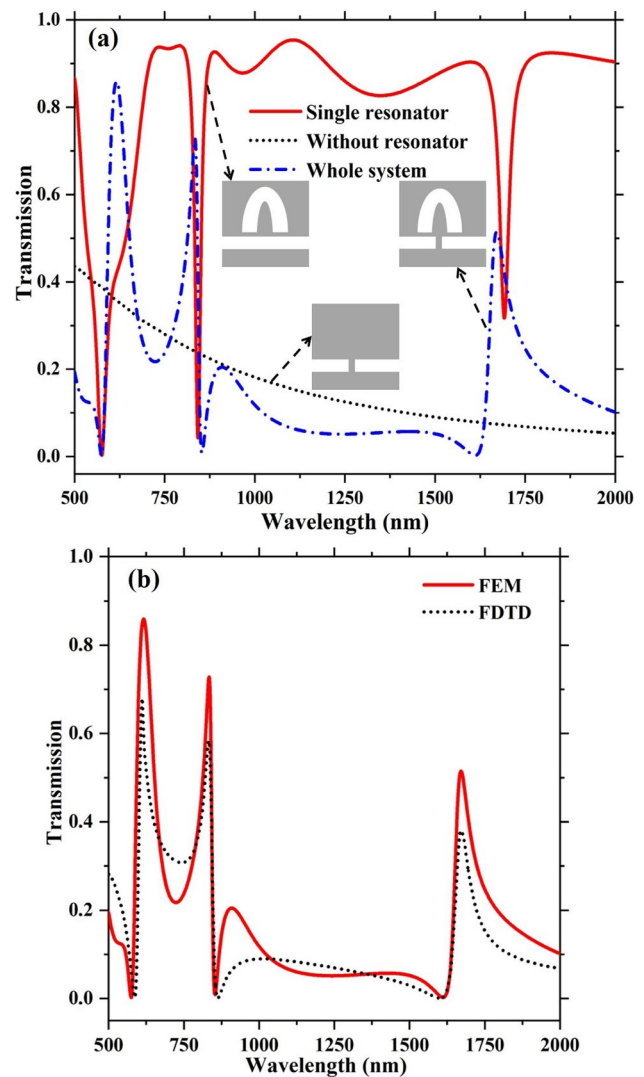

Fig. 2 **a** The obtained transmission spectra, without resonator (dotted black line), with single MIM SERR resonator (red solid line) and of the overall plasmonic system (dash dot blue line). **b** The comparison between transmission spectra obtained by the FEM (red solid line) and the FDTD (dotted black line) methods. The geometrical parameters of the structure are as follows: $w = 50\,nm$, $d = 10\,nm$, $g = 10\,nm$, $r = 105\,nm$, and $R = 225\,nm$

to three parts: the first one is without baffle, the second one is composed of MIM waveguide with baffle only, and the last one represents the whole structure. Initially, the geometrical parameters of the structure are defined as $R = 225 \, nm$, $r = 105 \, nm$, $d = 10 \, nm$, and $g = 10 \, nm$. As shown in Fig. 2a, for the structure without baffle (red solid line), there are three transmission dips (less than 0.04) at $\lambda_1 = 1692 \, nm$, $\lambda_2 = 842 \, nm$, and $\lambda_3 = 571 \, nm$ in the transmission spectrum, which can be treated as narrow discrete states. Meanwhile, the MIM waveguide with baffle can form a broad continuum state as indicated by the dotted black line in the transmission spectrum.

This observation is in good agreement with the resonance condition mentioned in the analytical Eq. (3). In addition, as shown by the blue (dash dot) spectral line produced by the overall structure, there are three sharp asymmetric resonance shapes that rapidly changed from peaks to dips. The spectral line shape is formed by a phenomenon produced by the interference of a broad continuous state (black dotted line) and a narrow discrete state (red solid line) which is called the Fano resonance. The transmission values of the triple Fano resonance peaks are about $T_{p1} = 0.52$ (for $\lambda_{p1} = 1668 \, nm$), $T_{p2} = 0.73$ (for $\lambda_{p2} = 833 \, nm$), and $T_{p3} = 0.87$ (for $\lambda_{p3} = 615 \, nm$). In order to consolidate the simulation results, a comparison between the transmission spectrum of the MIM waveguide structure obtained with the FEM and FDTD methods is presented in Fig. 2b. In this figure, the two spectra have almost the same general shape with a slight difference in intensity and a slight shift of the resonance peaks. These small differences can be explained to the different approaches of the two methods, such as meshing and boundary conditions (see reference [38]). What is left in this paper, all results will be obtained using the FEM method. The exact shape of the obtained Fano resonance profile depends indeed on the interaction between the discrete state and the continuum of states, this interaction being quantified by a phenomenological parameter q. The profile of the effective section of the observed physical phenomenon is given by [48]:

$$\sigma = \frac{(\epsilon + q)^2}{\epsilon^2 + 1} \tag{4}$$

where q is given by the ratio of the optical response of the localized state to the continuum that refers to the degree of resonance asymmetry. The reduced energy ϵ is defined by $\frac{2(E - E_F)}{\Gamma}$, E_F being the resonance energy and Γ the width of the self-ionized state. In the $|q| \rightarrow \infty$ limit, the shape of the line is entirely determined by the transition through the discrete state only with the standard "Lorentzian" profile. The case where $q = 0$ is unique to the Fano resonance and refers to a symmetric dip, sometimes called anti-resonance. In the case where $q < 0$, the direction of the asymmetric Fano line shape is negative; this is why the Fano line shape in Fig. 2a occurs at $\lambda_3 = 615 \, nm$ and $\lambda_1 = 1692 \, nm$ in such

a way that the Fano resonance peak is on the left, while the Fano resonance valley is on the right. In the case of $q > 0$, the shape of asymmetric Fano spectral is positive, that is why in Fig. 2a, the Fano resonance occurs at $\lambda_2 = 833 \, nm$ in a manner that the Fano resonance peak is on the left and the valley is on the right. To understand the internal mechanism of the resonance peak in the transmission spectrum, the $|H_z|$ distribution of the steady-state magnetic field of the proposed waveguide system was studied. Figure 3 shows the $|H_z|$ magnetic field distributions at the peaks and dips of the Fano resonances.

Figure 3b, c, e shows the $|H_z|$ distribution at wavelengths of 615 nm, 833 nm, and 1671 nm, respectively, where most of the SPPs are able to pass through the waveguide, while the SPPs are almost cancelled in the output port (P_2) as shown in Fig. 3a, d, f at wavelengths of 571 nm, 855 nm, and 1609 nm, respectively. In addition, there are two, three, and four nodes in the $|H_z|$ distribution for the Fano *FR1*, *FR2*, and *FR3* resonances, respectively. According to the number of nodes in the resonator wavelength (FP) [11], the three resonance modes of *FR1*, *FR2*, and *FR3* can be represented by TM_1 mode, $TM_{1.5}$ mode, and TM_2 mode, respectively; these resonance modes of the SERR resonator can be classified into symmetric modes (TM_1 and TM_2) and asymmetric mode ($TM_{1.5}$). This last observation is in good agreement with the resonance condition mentioned in the analytical Eq. (3). Afterwards, the mechanism of the Fano resonance at the peaks (615 nm, 833 nm, and 1671 nm) is discussed. The SPPs can travel through the input waveguide in Fig. 3b, c, e where the near field $|H_z|$ in the baffle oscillates in phase with the field $|H_z|$ of the input MIM waveguide and a strong field is confined in this baffle and the SERR resonator, which causes constructive interference and transmission
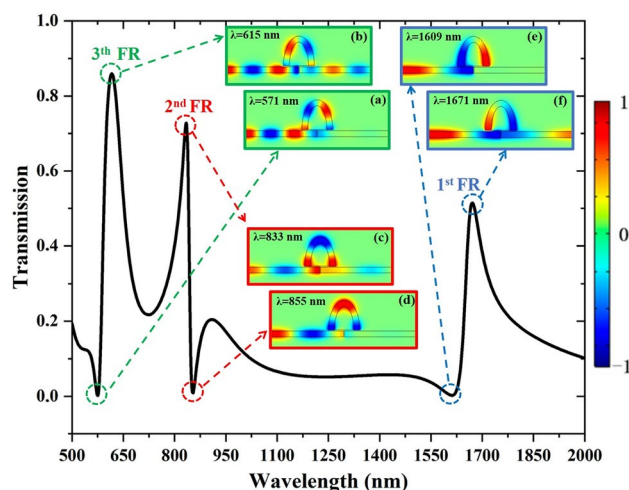

Fig. 3 The magnetic field distributions of the SERR structure at the peaks and dips of the triple Fano resonance: **a** $\lambda = 571 \, nm$, **b** $\lambda = 615 \, nm$, **c** $\lambda = 833 \, nm$, **d** $\lambda = 855 \, nm$, **e** $\lambda = 1609 \, nm$, **f** $\lambda = 1671 \, nm$

enhancement. Furthermore, the magnetic field profile $|H_z|$ for the plasmonic system at the dip wavelength is shown in Fig. 3a, d, f, where the $|H_z|$ field in the baffle is well coupled and oscillates in anti-phase with the $|H_z|$ field of the input MIM waveguide. In the last case, the destructive interference occurs, leading to transmission cut-off, where most of the input SPPs cannot cross the bus waveguide.

According to the above discussions, when there is no single metal baffle, TM_0 waves penetrate into the waveguide bus, and a narrower discrete state is formed by using the SERR resonator. In this case, the transmission spectrum satisfies the standing wave resonance condition at a certain frequency. As a result, when both states occur at the same time, the Fano resonance will be produced by the coupling between the wider continuous state and the narrower discrete state under the near-field interaction, where destructive interference occurs when the continuous state and the discrete states are coupled to each other on the transmission spectrum, causing an asymmetric Fano resonance line in the transmission spectrum. As shown in Fig. 3, it can be known that the three Fano resonances are caused by a coupling effect resulting from the SERR elliptical resonator and the metal baffle. Meanwhile, the resonance mode is confined and distributed along the effective perimeter of the SERR resonator depending on the baffle width and the coupling distance, so that the adjustment of these parameters will change the wavelength and transmission intensity of the resonance. In the following section, the effect of these parameters will be investigated.

The Influence of Geometrical Parameters

The influence of MIM waveguide geometrical parameters on system characteristics was studied. As was indicated previously, Fano resonance is an asymmetric Lorentzian line formed by the coupling between a wider continuous state created by the baffle and a narrower discrete state generated by the SERR; thus, changing their geometrical parameters will have a certain influence on the position and line shape of Fano resonances.

First, we analyze the effects of different coupling distance g on sensor properties. The coupling distance directly affects the coupling effect between the discrete state and the continuous state; thus, the influence of coupling distance g on Fano resonance is analyzed, which was investigated in Fig. 4. This figure represents the transmission spectra of the proposed structure at the three Fano resonance modes with different coupling gap distances g. We changed coupling distance g from 10 to 35 nm in steps of 5 nm, and the other structural parameters were kept changeless which are set at $R = 225 \, nm$, $r = 105 \, nm$, and $d = 10 \, nm$. For the represented Fano resonances, it can be seen that the transmittance tends

to decrease as the coupling distance g increases. For the resonance peak *FR1*, it has a blue shift with the increase of g, while for the others resonance peaks, wavelengths still basically remain unchanged, and their profiles are roughly the same. This is due to the attenuation of the coupling between the discrete narrow-band state excited by the SERR and the continuous broadband state created by the baffle as it moves away from the bus waveguide. To obtain both a higher transmission peak and sharp Fano line shape which is suitable spectra for sensing application and also to take into account the constraints of accuracy of the manufacturing process, the distance of the coupling gap can be chosen close to 10 nm. Therefore, the distance g was considered to be 10 nm in all simulations in this section. We suggest within the next study to investigate the effect of the SERR radii on the waveguide transmission spectra.

Moreover, the effect of the width d of the silver baffle on the excited Fano resonance is discussed. The geometrical parameters are $R = 225 \, nm$, $r = 105 \, nm$, and $g = 10 \, nm$ where d is increased from 10 to 160 nm with a step of 20 nm as shown in Fig. 5. This figure indicates that for the Fano resonances *FR1* and *FR2*, when the width d increases, both the resonant wavelength and the transmission at peaks remain basically unchanged, i.e., they are not sensitive to the change of the parameter d. While that increasing the distance d will change the shape of the curves more obviously, which transformed an almost asymmetrical shape into an entirely symmetrical shape (Lorentzian). For the Fano resonance *FR3*, the transmission spectra decreases gradually, and the curves transformed from an almost asymmetrical shape into an entirely symmetrical shape without a significant influence of this distance on the resonance wavelength of this Fano resonance.

Likewise, the effect of main radii R and r on the transmission spectra will be discussed also. By independently varying both the main radii R and r of the SERR resonator where the remaining parameters are the same as in Fig. 3, the obtained results are shown in Fig. 6. As shown in Fig. 6a, on the one hand, the wavelength of the Fano resonances of the investigated plasmonic system exhibits a linear red-shift when the radius R of the resonator increases from 80 to 280 nm, with a linear increase in the transmission of the *FR1* resonance peak. For the Fano resonances *FR2* and *FR3*, the spectrum shape gradually transforms from an almost symmetrical (Lorentzian-like) shape to an asymmetrical Fano-like shape with increasing radius R. On the other hand, the wavelength of the Fano resonances produced by the SERR resonator shows a simultaneously significant red-shift when the radius r increases from 80 to 280 nm with a decrease of the transmission intensity at the the Fano *FR1* and *FR2* resonance peaks, but at the Fano *FR3* resonance, it undergoes to a progressive increase up to the value $T_{p3} = 0.87$ at $\lambda_3 = 571 \, nm$. For the Fano *FR3* resonance, the shape of the spectrum is

Fig. 4 **a** Transmission spectra with different values of the gap *g* ranging from 10 to 35 *nm*. **b** The resonant wavelength and the transmission of Fano resonance peak as a function of the coupling distance. The other geometrical parameters are $R = 225\,nm$, $r = 105\,nm$, and $d = 10\,nm$
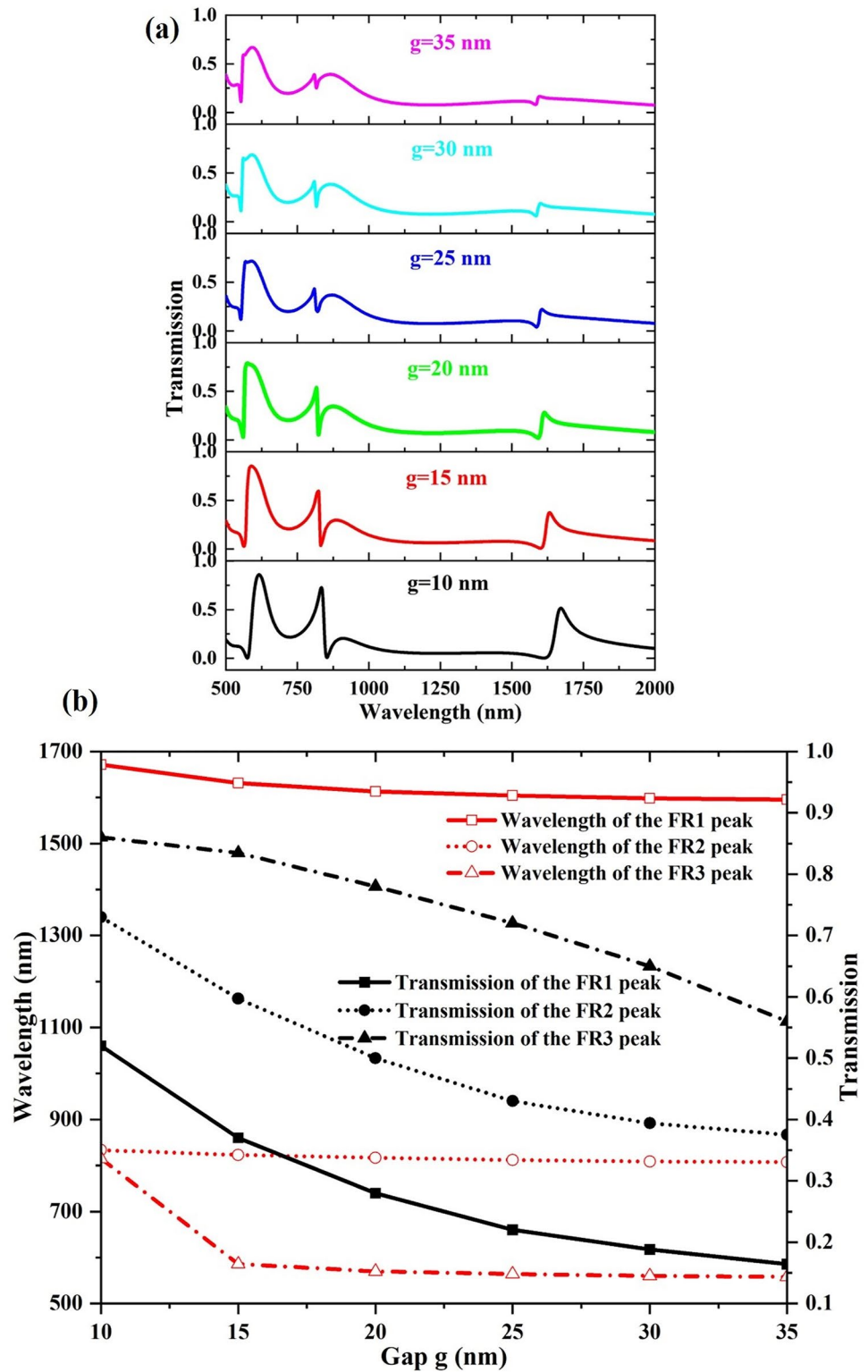
gradually transformed from an almost symmetrical shape (Lorentzian type) to an asymmetrical Fano type shape with the increase of the minor radius *r*.

Consequently, the use of a semi-elliptical ring resonator offers greater adjustability in the transmission characteristics of the MIM waveguide structure. By changing the geometrical parameters of the proposed structure, the Fano resonances shapes can be easily adjusted spectrally. The optimized geometrical parameters of the structure are as follows: $w = 50\,nm$, $d = 10\,nm$, $g = 10\,nm$, $r = 105\,nm$, and $R = 225\,nm$
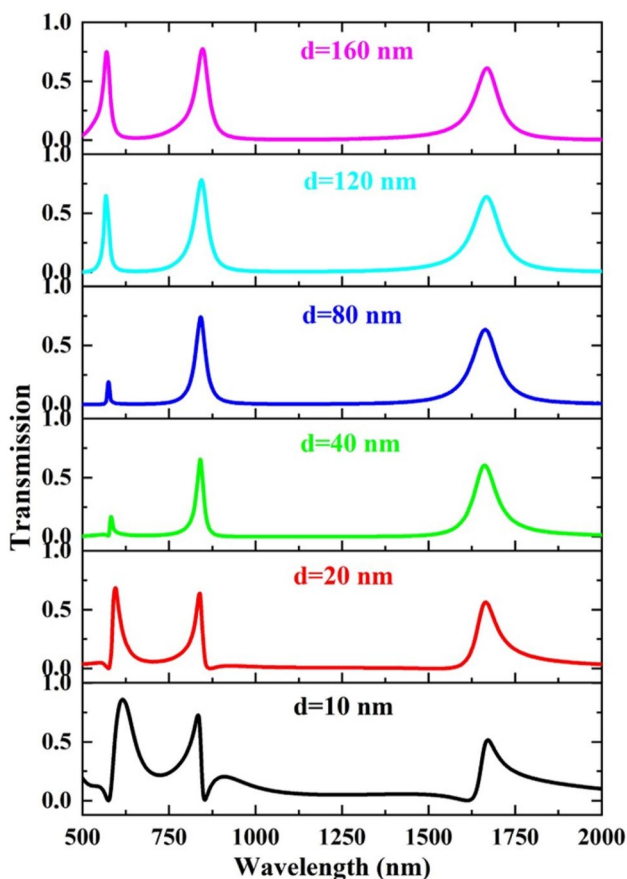
Fig. 5 Transmission spectra with different values of the metallic baffle width *d* ranging from 10 to 160 *nm*. The other geometrical parameters are *R* = 225 *nm*, *r* = 105 *nm*, and *g* = 10 *nm*

Sensing Applications Based on Fano Resonances

The MIM plasmonic waveguide-based Fano system has great potential as a highly integrated refractive index sensor due to its asymmetric spectral shape, where the transmission can drop sharply from the peak to the valley (dip) of the spectrum. Such a short wavelength change can provide an ultra-narrow transmission peak, which can greatly increase the resolution of refractive index sensing (a biochemical sensor for example). As shown in Fig. 7, initially, we assume that the refractive index of the detected insulator has a value of *n* = 1, and subsequently, it is changed from 1 to 1.06.

Figure 8a–c shows that the spectrum of the investigated structure for the three Fano resonances has a shift towards infrared frequencies with the increase of the refractive index of the dielectric medium. The line shape almost unchanged, which exhibits good switching properties. In addition, there is a linear relationship between resonance wavelength and refractive index, which is a key factor for the design of a high-performance sensor. To evaluate the performance of the sensor, we measure two parameters: sensitivity (S) and figure of merit (FOM). Sensitivity (S) is an important performance index to quantitatively evaluate and characterize the nanoscale refractive index sensor, which is usually defined as the ratio of wavelength change caused by the unit change of refractive index. It is calculated using the following expression [49]:

$$S = \frac{\Delta \lambda}{\Delta n} \tag{5}$$

Fig. 6 **a** Transmission spectra with different values of the radius *R* ranging from 80 to 280 *nm* (when *r* = 105 *nm*). **b** Transmission spectra with different values of the radius *r* ranging from 80 to 280 *nm* (when *r* = 105 *nm*). The other geometrical parameters are *g* = 10 *nm* and *d* = 10 *nm*
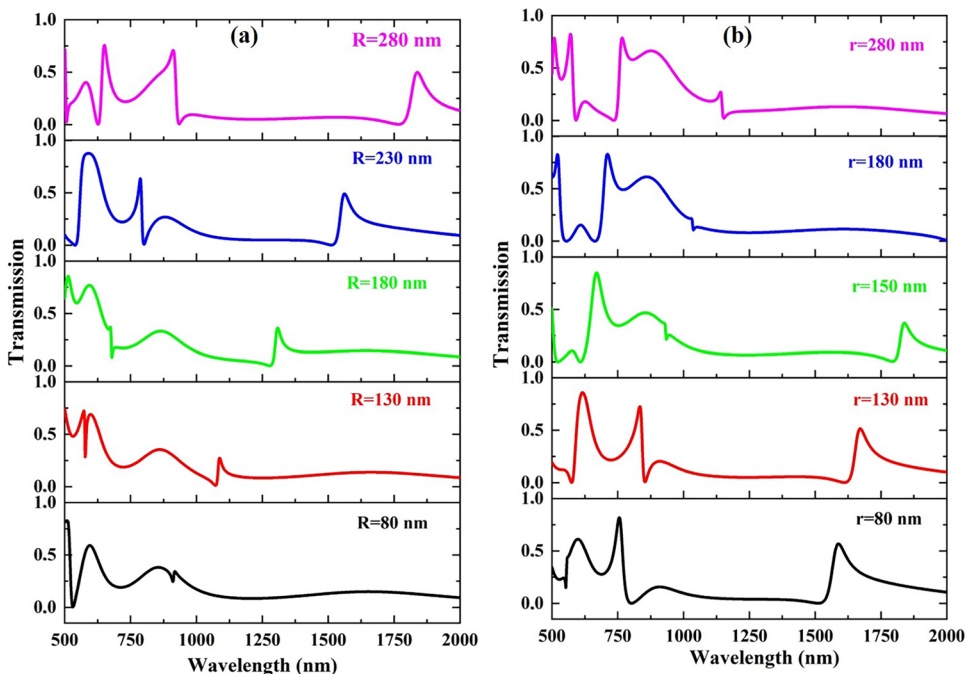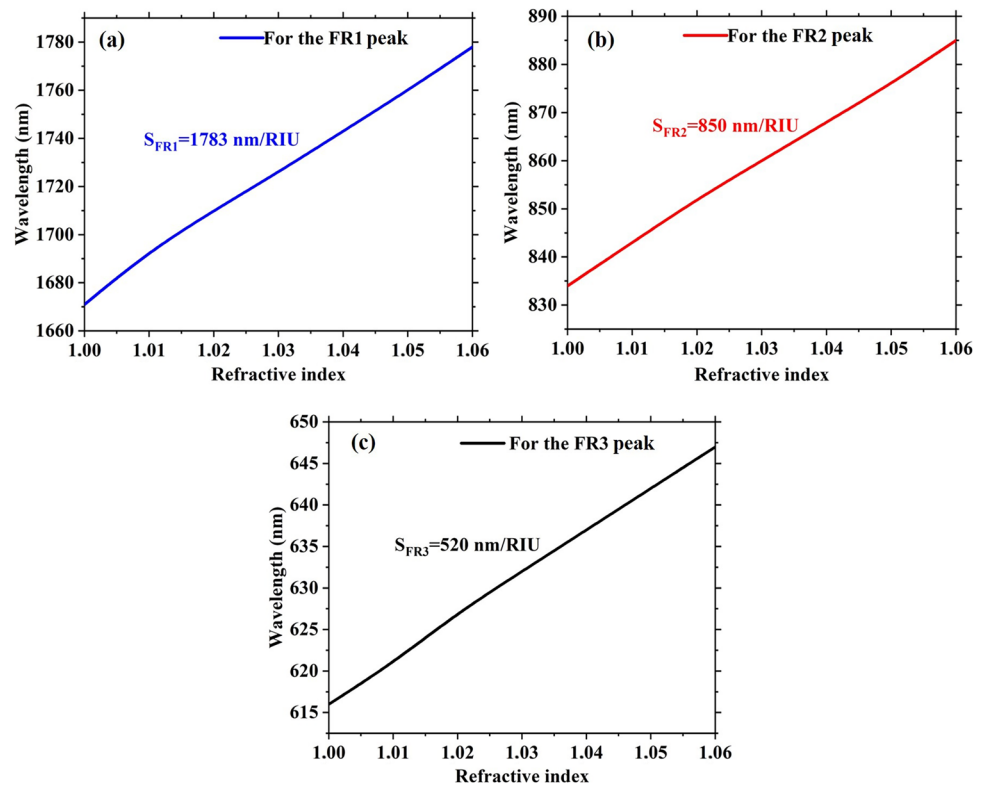
Fig. 7 Transmission spectra of the SERR structure with $g = 10$ nm, $d = 10$ nm, $R = 225$ nm, and $r = 105$ nm for different values of the refractive index of the dielectric

where Δn is the change in refractive index unit (*RIU*) and $\Delta \lambda$ is the change in wavelength. The calculated sensitivity around the *FR1*, *FR2*, and *FR3* resonance peaks is approximately $S_{FR1} = 1783$ *nm/RIU*, $S_{FR2} = 850$ *nm/RIU*, and $S_{FR3} = 520$ *nm/RIU*, respectively. In addition, to further evaluate the characteristics and performance of the

plasmonic sensor, we investigated the figure of merit (FOM) which is another important parameter used to quantify the performance of the nanoscale refractive index sensor. It is defined as the ratio between the sensitivity of the sensor and the bandwidth of the resonance (i.e., FWHM: full width at half maximum). If the FWHM also increases significantly,

Fig. 8 The different Fano peak wavelength versus the refractive index: **a** for the Fano *FR*1 resonance peak, **b** for the Fano *FR*2 resonance peak, **c** for the Fano *FR*3 resonance peak

729
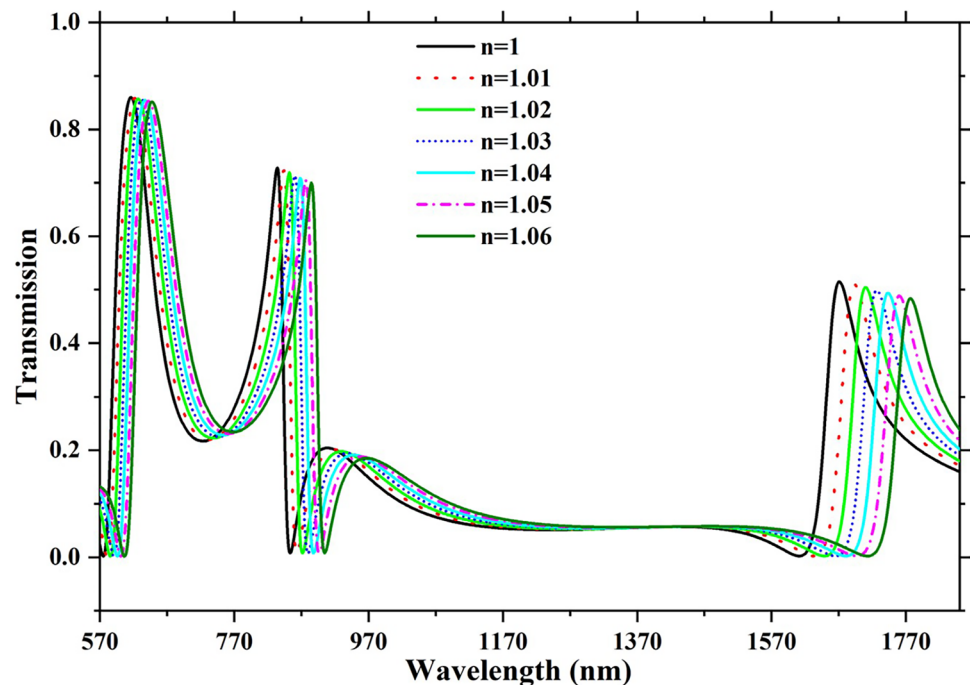
this will result in a reduction in the FOM of the sensor. The faster the relative transmission intensity changes, the more easily the transmission spectrum change can be detected. For a sensing application, FOM is commonly applied to further estimate the sensing performance of the sensor and is calculated by the following expression [49]:

$$FOM = \frac{S}{FWHM} \tag{6}$$

The FOM values of the proposed structure are obtained around the three Fano resonances as follows: $FOM_{FR1} = 25.5$ RIU^{-1}, $FOM_{FR2} = 27$ RIU^{-1}, and $FOM_{FR3} = 9$ RIU^{-1}. Table 1 summarizes a comparison of the sensitivity and figure of merit (FOM) values obtained in this work with previous works. This comparison shows that the investigated structure has improved results compared to other recently published works.

Slow Light Effect

The slow light effect is one of the most important applications reported by many papers. The waveguide structure designed in this paper also supports the slow light effect due to the sharp line shape of the Fano resonance. To get more insight to the physical characters of slow light effect, it can be evaluated by the group delay time $\tau_g(ps)$) and the group index n_g, which are expressed by [57]:

$$\tau_g = \frac{d\psi(\omega)}{d\omega} = -\frac{\lambda^2}{2\pi c}\frac{d\psi(\lambda)}{d\lambda} \tag{7}$$

$$n_g = \frac{c}{V_g} = \frac{c}{L_0}\tau_g = -\frac{\lambda^2}{2\pi L_0}\frac{d\psi(\lambda)}{d\lambda} \tag{8}$$

Here, c is the speed of light in free space, and v_g stands for the group velocity in the plasmonic waveguide systems. τ_g and $\psi(\lambda)$) are the optical delay time and transmission

Table 1 Comparisons of results (sensitivity and FOM) with previous recent research

Reference/year	FOM (RIU^{-1})	Sensitivity (nm/RIU)
This work	27	1783
[50] 2023	48.17	1132.14
[51] 2022	15.85	1647
[52] 2023	11.84	900
[53] 2020	43.05	1550
[54] 2022	29	1007.78
[55] 2022	108.36	1050
[56] 2020	14.83	1556

phase shift, respectively. $L_0 = 1500$ nm is the length of the plasmonic system, and λ is the wavelength of transmitted optical signal.

After a detailed study where we changed the different geometrical parameters of the structure (this study is not represented in this paper), the optimal parameters to obtain significant values of the optical delay and the group index are $R = 225$ nm, $r = 105$ nm, $d = 10$ nm, and $g = 10$ nm. The calculated results are shown in Fig. 9. This figure shows the phase shift and the correspondent optical delay as a function of wavelength, from which it can be seen that there is a rapid phase change around the Fano transmission profile due to the rapid phase change when the SPP resonance takes place. The phase slope near the Fano trough is positive, and there is a large abnormal dispersion, while the phase slope near the Fano peak is negative where there is a large normal dispersion. These observations show that the designed structure can achieve both fast and slow light effects. As a result, the negative group delay (or negative group index) and positive group delay (or positive group index) are obtained in the Fano dips and peaks, respectively, where the maximum positive group delay is about 0.887 ps and the corresponding maximum group index is about 20.5. This means that this plasmonic device can delay a light wave for a duration of 0.887 ps around the $\lambda_{p1} = 1668$ nm peak.

Table 2 summarizes a comparison of the optical delay values obtained in this work with previous works. This comparison shows that the investigated structure has enhanced results compared to other recently published works, and the presented work provides a simple method for the realization of highly integrated plasmonic devices which has potential applications on slow light, such as optical switches and optical memories.
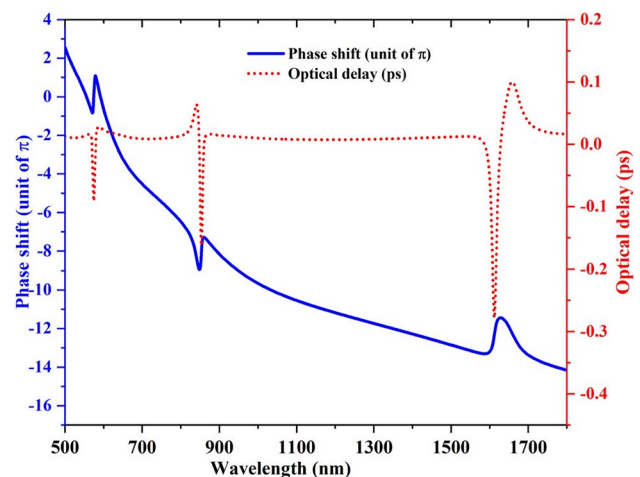

Fig. 9 Transmission phase shift (blue solid line) and optical delay (red dotted line) of the plasmonic system, with $R = 225$ nm, $r = 105$ nm, $d = 10$ nm, and $g = 10$ nm and $D = 1.5$ μm (Structure length)

Table 2 Comparison of the characteristics of the proposed slow light plasmonic devices structures based on optical delay, group index, and the cavity structure reported in the literature

Ref/year	Simulation method	Structure design	Detection range	Optical delay (*ps*)
This work	FEM	Semi-elliptical ring resonator	Near-infrared	0.887
[58] 2019	FDTD	MIM coupled cavities system	Visible/near-infrared	~0.14, ~0.08, and ~0.08
[59] 2020	FDTD	End-coupled slot cavity with multiple output MIM ports	Visible	0.14
[60] 2019	FDTD	Rectangular cavity and an inverted U-shaped groove	Visible/near-infrared	~0.077, ~0.146, ~0.110, and ~0.085
[61] 2021	FEM	Circular split-ring resonance cavity and a double symmetric rectangular stub waveguide	Visible	0.128
[62] 2020	FEM	Slotted side-coupled disk resonator	Near-infrared	0.34
[63] 2022	FDTD	Cross-shape rectangular cavity	Near-infrared	~0.35 and ~0.18
[64] 2019	FDTD	Side-coupled elliptical resonator	Visible	0.05
[65] 2019	FDTD	Semi-ring-rectangular composite cavity	Near-infrared	~0.167, ~0.0955, ~0.0958, and ~0.0389
[66] 2018	FDTD	End-coupled slot cavity resonator	Visible/near-infrared	0.05 and 0.07
[67] 2021	FDTD	Dual tooth cavities coupled with stub resonators separately	Near-infrared	0.074
[68] 2018	FEM	Semi-elliptical ring resonator	Near-infrared	0.04

Conclusion

In conclusion, a MIM-type surface plasmon optical waveguide composed of a SERR and a baffle is designed. The Fano resonance of the structure is formed by the interference of the narrow-band discrete state triggered by the SERR and the wide-band continuous state excited the same way by the baffle. The simulation results show that the structure excites triple Fano resonances. The resonance wavelength and spectrum line shape of the Fano resonance can be tuned by the geometrical parameters of the structure. After optimizing these parameters, the sensitivity and the FOM of the designed system can reach up to 1783 *nm*/*RIU* and 27, respectively. This structure can also come up to a maximum optical delay of about 0.887 *ps*. Based on the previous results, the structure has more geometric parameters and more flexible tunability, which makes the designed MIM waveguide structure having potential application prospects in the fields of RI sensors and slow light devices.

Author Contributions Mustapha Figuigue conceived of the presented idea and performed the comparison with the other numerical method (FDTD). Rida El Haffar performed the computations and the comparison with other works. Oussama Mahboub verified the analytical methods, defined the characterization concept, and supervised the findings of this work. All authors discussed the results and contributed to the final manuscript.

Data Availability The authors confirm that the data supporting the findings of this study are available within the article.

Declarations

Ethical Approval Not applicable.

Consent to Participate All authors gave their consent to participate.

Consent for Publication All authors gave their consent for publication.

Conflict of Interest The authors declare no competing interests.

References

1. Barnes WL, Dereux A, Ebbesen TW (2003) Surface plasmon subwavelength optics. Nature 424(6950):824–830
2. Noual A, Kang E, Maji T, Gkikas M, Djafari-Rouhani B, Fytas G (2021) Optomechanic coupling in Ag polymer nanocomposite films. J Phys Chem C 125(27):14854–14864
3. Gramotnev DK, Bozhevolnyi SI (2010) Plasmonics beyond the diffraction limit. Nature Photon 4(2):83–91
4. Saada TN, da Silva AGM, Subramanian P, Pang L, Adnane N, Djafari-Rouhani B, ... Szunerits S (2020) Plasmon-enhanced electrocatalytic oxygen reduction in alkaline media on gold nanohole electrodes. J Mater Chem A 8(20):10395–10401
5. Mondir A, Setti L, El Haffar R (2022) Design, analysis, and modeling using WCIP method of novel microstrip patch antenna for THz applications. Progress In Electromagnetics Research C 125:67–82
6. El Haffar R et al (2022) All-optical logic gates using a plasmonic MIM waveguide and elliptical ring resonator. Plasmonics 1-12
7. Sarkaleh AK, Lahijani BV, Saberkari H, Esmaeeli A (2017) Optical ring resonators: a platform for biological sensing applications. J Med Signals Sens 7:185–191
8. Tsigaridas GN (2017) A study on refractive index sensors based on optical micro-ring resonators. Photonic Sens 7:217–225

9. Zhang Z, Shi F, Chen Y (2015) Tunable multichannel plasmonic filter based on coupling-induced mode splitting. Plasmonics 10:139–144

10. Wang S, Li Y, Xu Q, Li S (2016) A MIM filter based on a side-coupled crossbeam square-ring resonator. Plasmonics 11:1291–1296

11. Ma F, Lee C (2013) Optical nanofilters based on meta-atom side-coupled plasmonics metal-insulator-metal waveguides. J Lightwave Technol 31:2876–2880

12. Veronis G, Fan S (2005) Bends and splitters in metal-dielectric-metal subwavelength plasmonic waveguides. Appl Phys Lett 87

13. Yan X, Wang T, Han X, Xiao S, Zhu Y, Wang Y (2017) High sensitivity nanoplasmonic sensor based on plasmon-induced transparency in a graphene nanoribbon waveguide coupled with detuned graphene square-nanoring resonators. Plasmonics 12:1449–1455

14. Peng B, Özdemir SK, Chen W, Nori F, Yang L (2014) What is and what is not electromagnetically induced transparency in whispering-gallery microcavities. Nat Commun 5:5082–5092

15. Zhang ZD, Wang HY, Zhang ZY (2013) Fano resonance in a gear-shaped nanocavity of the metal-insulator-metal waveguide. Plasmonics 8:797–801

16. Yu S, Piao X, Hong J, Park N (2015) Progress toward high-Q perfect absorption: a Fano antilaser. Phys Rev A 92:011802

17. Limonov MF, Rybin MV, Poddubny AN et al (2017) Fano resonances in photonics. Nat Photon 11(9):543–54

18. Miroshnichenko A, Flach S, Kivshar Y (2010) Fano resonances in nanoscale structures. Rev Mod Phys 82(3):2257–2298

19. Zhang Y, Cui M (2019) Refractive index sensor based on the symmetric MIM waveguide structure. J Electron Mater 48:1005–10

20. Liu Z, Liu G, Huang S, Liu X, Pan P, Wang Y, Gu G (2015) Multispectral spatial and frequency selective sensing with ultra-compact cross-shaped antenna plasmonic crystals. Sens Actuators B Chem 215:480–488

21. Asadi R, Malek-Mohammad M, Khorasani S (2011) All optical switch based on Fano resonance in metal nanocomposite photonic crystals. Opt Commun 284(8):2230–5

22. Amin M, Ramzan R, Siddiqui O (2017) Fano resonance based ultra-high-contrast electromagnetic switch. Appl Phys Lett 110(18)

23. Zhan S, Peng Y, He Z et al (2016) Tunable nanoplasmonic sensor based on the asymmetric degree of Fano resonance in MDM waveguide. Sci Rep 6(1):22428

24. Piao X, Yu S, Park N (2012) Control of Fano asymmetry in plasmon induced transparency and its application to plasmonic waveguide modulator. Opt Express 20(17):18994

25. Kazanskiy NL, Khonina SN, Butt MA (2020) Plasmonic sensors based on Metal-insulator-metal waveguides for refractive index sensing applications: a brief review. Phys E 117:113798

26. Butt A, Khonina SN, Kazanskiy NL (2019) A multichannel metallic dual nano-wall square split-ring resonator: design analysis and applications. Laser Phys Lett 16(12)

27. Chen J, Li Z, Zou Y, Deng Z, Xiao J, Gong Q (2013) Coupled-resonator-induced Fano resonances for plasmonic sensing with ultra-high figure of merits. Plasmonics 8:1627–1631

28. Wen KH, Hu YH, Chen L, Zhou JY, Lei L, Guo Z (2015) Fano resonance with ultra-high figure of merits based on plasmonic metal-insulator-metal waveguide. Plasmonics 10:27–32

29. Lu H, Liu X, Mao D, Wang G (2012) Plasmonic nanosensor based on Fano resonance in waveguide-coupled resonators. Opt Lett 37:3780–3782

30. Wang Q, Ouyang ZB, Lin M, Liu Q (2018) independently tunable Fano resonance based on the coupled hetero cavities in a plasmonic MIM system. Materials 11:1675

31. Meng ZM, Li ZY (2018) Control of Fano resonance in photonic crystal nanobeams side coupled with nanobeam cavities and their applications to refractive index sensing. J Phys D Appl Phys Accept

32. An HL, Zhang GM, Hu N, Shi Y, Wang ZS (2016) Phenomenon of multiple Fano resonances based on coupled T-type cavity. Acta Photonica Sin 45(11):112–117

33. Fang YH, Wen KH, Qin YW, Li ZF, Wu B (2019) Multiple Fano resonances in an end coupled MIM waveguide system. Opt Commun 452

34. Qi Y et al (2022) Tunable plasmon refractive index sensor and slow light characteristics based on a stub coupled with an ellipse resonator and its derived structure. JOSA B 39(11):2957–2968

35. Panindre P, Kumar S (2016) Effect of rounding corners on optical resonances in single-mode sharp-cornered microresonators. Opt Lett 41:878–881

36. Tian M, Lu P, Chen L, Lv C, Liu DM (2011) A subwavelength MIM waveguide resonator with an outer portion smooth bend structure. Opt Commun 284(16–17):4078–4081

37. Cai Y, Li Y, Nordlander P, Cremer PS (2012) Fabrication of elliptical nanorings with highly tunable and multiple plasmonic resonances. Nano Lett 12:4881–4888

38. Yurkin MA (2013) Computational approaches for plasmonics. In Handbook of molecular plasmonics. ed. by F. Della Sala, S. D'Agostino. Pan Stanford Publishing, Singapore pp. 83-135

39. Stade F, Heeren A, Fleischer M, Kern DP (2007) Fabrication of metallic nanostructures for investigating plasmon-induced field enhancement. Microelectron Eng 84:1589–1592

40. Campos A, Arbouet A, Martin J, Gerard D, Proust J, Plain J, Kociak M (2017) Plasmonic breathing and edge modes in aluminum nanotriangles. ACS Photonics 4:1257–1263

41. Bozhevolnyi SI, Volkov VS, Devaux E, Laluet JY, Ebbesen TW (2006) Channel plasmon subwavelength waveguide components including interferometers and ring resonators. Nature 440:508–511

42. Vesseur EJR, Waele RD, Lezec HJ, Atwater HA, Garcia de Abajo FJ, Ploman A (2008) Surface plasmon polaritons modes in a single crystal Au nanoresonator fabricated using focused-ion-beam milling. Appl Phys Lett 92:083110-1-083110–3

43. Hocini A, Ben Salah H, Temmar MN (2021) Ultra-high-sensitive sensor based on a metal-insulator-metal waveguide coupled with cross cavity. J Comput Electron 20(3):1354–1362

44. Jung Woo Kyung, Byun Kyung Min (2011) Fabrication of nanoscale plasmonic structures and their applications to photonic devices and biosensors. Biomed Eng Lett 1:153–162

45. Shibayama J, Kawai H, Yamauchi J, Nakano H (2019) Analysis of a 3D MIM waveguide-based plasmonic demultiplexer using the TRC-FDTD method. Opt Commun 452:360–365

46. Han Z, He S (2007) Two-dimensional model for three-dimensional index-guided multimode plasmonic waveguides and the design of ultrasmall multimode interference splitters. Appl Opt 46(25):6223–6227

47. Chen Z et al (2015) Tunable electromagnetically induced transparency in plasmonic system and its application in nanosensor and spectral splitting. IEEE Photon J 7(6):1–8

48. Gallinet B, Martin OJF (2011) Influence of electromagnetic interactions on the line shape of plasmonic Fano resonances. ACS Nano 5:8999–9008

49. Ahmadivand A, Karabiyik M, Pala N (2015) Inducing multiple Fano resonant modes in split concentric nanoring resonator dimers for ultraprecise sensing. J Opt 17(8)

50. Butt MA, Kazanskiy NL, Khonina SN (2023) Tapered waveguide mode converters for metal-insulator-metal waveguide plasmonic sensors. Measurement 211

51. Abbasi H (2022) Design of a plasmonic refractive index sensor based on the amplifier system with two plasmonic waveguides and four cavities with different dimensions and coordinates. World J Clin Med Img 1(1)76, 80

52. Butt MA (2023) Numerical assessment of a metal-insulator-metal waveguide-based plasmonic sensor system for the recognition of tuberculosis in blood plasma. Micromachines 14(4):729

53. Su H et al (2020) Sensing features of the Fano resonance in an MIM waveguide coupled with an elliptical ring resonant cavity. Appl Sci 10(15):5096

54. Adhikari R et al (2022) Compact and sensitive H-shaped metal-dielectric-metal waveguide plasmonic sensor. Plasmonics 17(4):1593–1606

55. Khani S, Hayati M (2022) Optical sensing in single-mode filters base on surface plasmon H-shaped cavities. Opt Commun 505:127534

56. Sagor RH et al (2020) Numerical investigation of an optimized plasmonic on-chip refractive index sensor for temperature and blood group detection. Results in Physics 19

57. Lu H, Liu X, Mao D (2012) Plasmonic analog of electromagnetically induced transparency in multi-nanoresonator-coupled waveguide systems. Phys Rev A 85(5)

58. Li Z et al (2019) Control of multiple Fano resonances based on a subwavelength MIM coupled cavities system. IEEE Access 7:59369–59375

59. Fang Y et al (2020) Plasmonic refractive index sensor with multi-channel Fano resonances based on MIM waveguides. Mod Phys Lett B 34(16):2050173

60. Fang Y et al (2019) Multiple Fano resonances in an end-coupled MIM waveguide system. Optics Commun 452:12–17

61. Chen J et al (2021) Fano resonance in a MIM waveguide with double symmetric rectangular stubs and its sensing characteristics. Optics Commun 482:126563

62. Yu S et al (2020) Tunable plasmonic system based on a slotted side-coupled disk resonator and its multiple applications on chip-scale devices. Optik 212

63. Guo Z et al (2022) A plasmonic refractive-index sensor based multiple Fano resonance multiplexing in slot-cavity resonant system. Photonic Sensors 1-10

64. Zhang Z et al (2019) A plasmonic ellipse resonator possessing hybrid modes for ultracompact chipscale application. Physica Scripta 94(12)125511

65. Fang Y et al (2019) Multiple Fano resonances based on end-coupled semi-ring rectangular resonator. IEEE Photonics J 11(4):1–8

66. Wen K et al (2018) A plasmonic chip-scale refractive index sensor design based on multiple Fano resonances. Sensors 18(10):3181

67. Xie Y et al (2021) A tunable slow light device with multiple channels based on plasmon-induced transparency. Plasmonics 16:1809–1816

68. Yi X, Tian J, Yang R (2018) Tunable Fano resonance in MDM stub waveguide coupled with a U-shaped cavity. Eur Phys J D 72:1–9